UDC 551.515.21:551.509.313

# EXPERIMENTS WITH A NUMERICAL MODEL OF TROPICAL CYCLONE DEVELOPMENT

## Some Effects of Radial Resolution

STANLEY L. ROSENTHAL

Atlantic Oceanographic and Meteorological Laboratories, National Hurricane Research Laboratory, ESSA, Miami, Fla.

ABSTRACT

The model assumes the storm to be circularly symmetric and is expressed in $z$-coordinates. The information levels correspond to pressures in the mean tropical atmosphere of 1015, 900, 700, 500, 300, 200, and 100 mb. The heating function for the cyclone-scale motion is simulated by a convective adjustment of the lapse rate towards a pseudoadiabat representative of ascent from the surface boundary layer. The rate of this adjustment is calibrated so that the vertically integrated heating function is related to the upward flux of water vapor through the surface boundary layer.

Experiments with 10- and 20-km radial resolution are compared. The 10-km calculation yields a storm with more realistic structure. The 20-km case does not contain a well-defined eye, whereas the 10-km experiment does. Rainfall, kinetic energy production, and efficiency are all larger with 20-km resolution. In both experiments, computational damping is an important component of the kinetic energy budget; however, the total dissipation of kinetic energy (computational plus explicit) is fairly reasonable in comparison to that found in empirical studies.

## 1. INTRODUCTION

A recent report (Rosenthal 1969) described our tropical cyclone model and showed the results of a preliminary calculation (experiment I). We concluded that the model could simulate the life cycle of tropical cyclones with some degree of reality despite obvious deficiencies. Prominent among these was the rather coarse radial resolution (20 km between grid points) that had been adopted for computational economy.

For purposes of comparison, the results of an experiment with 10-km resolution are presented here. Because economic considerations dictate that we continue to use 20-km resolution for test calculations, this material is an important benchmark for assessing the effects of resolution errors.

## 2. REVIEW OF THE MODEL

The model proposed below differs from Ooyama's (1967) in that it employs primitive rather than balanced equations and has substantially greater vertical resolution. In contrast to Yamasaki's (1968) primitive equation model, our model uses "$z$" rather than "$p$" coordinates. Also, our system is open at the lateral boundary, whereas Yamasaki's is closed. The information levels are listed in table 1; all dependent variables are defined at all levels.

The $z$-system seems a natural one for the hurricane problem because of the very large pressure gradients that occur at low levels. Calculations below sea level that arise with pressure coordinates are avoided in the $z$-system. The "sigma" system of Phillips (1957), which might be a reasonable compromise between the $p$- and $z$-systems, leads to more complicated prognostic equations than those obtained below and, hence, is more costly from a computational point of view.

The primary source of energy for the development of tropical cyclones is the release of latent heat in organized systems of cumulonimbi; a successful model must contain a reasonable parametric representation of this heating function. Our formulation contains ingredients suggested by previous investigators—in particular, Charney and Eliassen (1964); Kuo (1965); Ogura (1964); Ooyama (1967); Syoño and Yamasaki (1966); Yamasaki (1968)—and is justified in the next paragraph.

TABLE 1.—*Heights and mean pressures of the information levels. The mean pressures are approximate and are based on a mean hurricane season sounding (Hebert and Jordan 1959).*

| Level | Height (meters) | Mean pressure (millibars) |
|---|---|---|
| 1 | 0 | 1,015 |
| 2 | 1,054 | 900 |
| 3 | 3,187 | 700 |
| 4 | 5,898 | 500 |
| 5 | 9,697 | 300 |
| 6 | 12,423 | 200 |
| 7 | 16,621 | 100 |

The lower 400 to 500 mb of the undisturbed, marine tropical atmosphere is almost always conditionally unstable (Gray 1967, Hebert and Jordan 1959, Garstang et al. 1967, Malkus 1960). Empirical evidence (Gray 1967, Garstang et al. 1967, Malkus 1960) suggests that the organized systems of deep cumulonimbi associated with synoptic disturbances *tend* to neutralize this conditional instability by adjusting the lapse rate toward a pseudoadiabat representative of parcel ascent from near sea level. Furthermore, these organized systems of deep cumulonimbi seem to occur only in the presence of low-level mass convergence (Malkus 1960), and the compensation for this mass convergence appears to take the form of ascent in the convective clouds (Riehl and Malkus 1961).

Finally, there seems to be a close relationship between water vapor convergence in the lowest layers and the rate of precipitation (Ogura 1964; Syoño 1950, 1951; Syoño et al. 1951).

A heating function that is reasonably consistent with these observations may be written

$$\dot{Q}=\frac{\bar{\rho}_2 L w_2 \tilde{q}(T_c-T)}{\int_{z_a}^{z_b}\bar{\rho}(T_c-T)dz}, \tag{1}$$

provided that $w_2>0,\ T_c>T.$ Otherwise,

$$\dot{Q}=0. \tag{1a}$$

In these expressions, $L$ is the latent heat of evaporation, $\bar{\rho}_2$ is a standard density at level 2, $w_2$ is the cyclone-scale vertical motion at that level, $\tilde{q}$ is the average specific humidity for the layer between levels 1 and 2, $T_c$ is the temperature of a surface air parcel rising with constant equivalent potential temperature, $T$ is the actual air temperature, $z_a$ is the lifting condensation level of the surface air, and $z_b$ (the cloud top) is the level at which the pseudoadiabat, through the lifting condensation level, becomes cooler than the environment (Kuo 1965).

According to equation (1):

1) Convection occurs only in the presence of low-level convergence ($w_2>0$) and conditional instability for surface air parcels ($T_c>T$).

2) All the water vapor that converges in the boundary layer rises in convective clouds, condenses, and falls out as precipitation.

3) All the latent heat thus released is made available to the large-scale flow.

4) The vertical distribution of this heating is such that the large-scale lapse rate is adjusted toward the pseudoadiabat appropriate to ascent from the surface.

The experiments reported on here are based on a highly simplified version of a more general model. While carried out primarily to test certain features of the model, they yielded results that are reasonable enough to present at this time. The major simplifications are as follows:

1) The lifting condensation level of the surface air is assumed to be fixed for all time halfway between levels 1 and 2 (527 m).

2) The average specific humidity over the lowest 1054 m is assumed to be the average saturation value for this layer.

3) The vertical transport of momentum by small-scale eddies is neglected, except at the air-sea interface where it is treated as a drag effect.

4) The air-sea exchange of sensible heat is pragmatically simulated by the requirement that air temperature in the lowest 1054 m be steady state.

These assumptions and simplifications are made primarily for reasons of computational economy. However, some of them also eliminate the need for explicit formulations of relatively obscure physical processes. Items 1 and 2 eliminate the need for a water vapor conveyance equation. The lack of internal dissipation by vertical mixing—assumption 3—is partly compensated for by the use of one-sided space and time differences which provide an implicit internal dissipation. Assumption 4, although not satisfying from a theoretical point of view, is justifiable on empirical grounds and is also used by Yamasaki (1968). It eliminates the need for a temperature forecast at levels 1 and 2 and for an explicit formulation of the air-sea exchange of sensible heat.

The basic system of equations, assuming circular symmetry, is

$$\frac{\partial M}{\partial t}=-u\frac{\partial M}{\partial r}-w\frac{\partial M}{\partial z}-fru+\frac{1}{\bar{\rho}}\frac{\partial}{\partial z}\left(\bar{\rho}K_z\frac{\partial M}{\partial z}\right)+\frac{K_H}{r}\frac{\partial}{\partial r}\left\{r^3\frac{\partial}{\partial r}\left(\frac{v}{r}\right)\right\}, \tag{2}$$

$$\frac{\partial u}{\partial t}=-u\frac{\partial u}{\partial r}-w\frac{\partial u}{\partial z}+\frac{M}{r}\left(f+\frac{M}{r^2}\right)-\theta\frac{\partial\phi}{\partial r}+\frac{1}{\bar{\rho}}\frac{\partial}{\partial z}\left(\bar{\rho}K_z\frac{\partial u}{\partial z}\right)+\frac{K_H}{r^2}\frac{\partial}{\partial r}\left\{r^3\frac{\partial}{\partial r}\left(\frac{u}{r}\right)\right\}, \tag{3}$$

$$\frac{\partial\theta}{\partial t}=-u\frac{\partial\theta}{\partial r}-w\frac{\partial\theta}{\partial z}+\frac{c_pK_H}{r\phi}\frac{\partial}{\partial r}\left(r\frac{\partial\theta}{\partial r}\right)+\frac{\dot{Q}}{\phi}, \tag{4}$$

$$\frac{\partial\phi}{\partial z}=-\frac{g}{\theta}, \tag{5}$$

$$\frac{\partial\bar{\rho}w}{\partial z}=-\frac{1}{r}\frac{\partial\bar{\rho}ru}{\partial r}, \tag{6}$$

$$\phi=c_p\left(\frac{p}{P_0}\right)^{R/c_p}, \tag{7}$$

$$\theta\phi=c_pT,\ \text{and}\ M=rv. \tag{8}$$

The symbols are defined as follows:

| | |
|---|---|
| $r$ | radius, |
| $z$ | height, |
| $t$ | time, |
| $M$ | relative angular momentum, |
| $u$ | radial velocity, |
| $v$ | tangential velocity, |
| $w$ | vertical velocity, |
| $f$ | Coriolis parameter, |
| $\bar{\rho}=\bar{\rho}(z)$ | density of a reference tropical atmosphere, |
| $K_z$ | kinematic coefficient of eddy viscosity for vertical mixing, |
| $K_H$ | kinematic coefficient of eddy viscosity and conductivity for lateral mixing, |
| $\theta$ | potential temperature, |
| $c_p$ | specific heat capacity at constant pressure for dry air, |
| $\dot{Q}$ | condensation heating per unit time and mass appropriate to the cyclone-scale flow, |
| $g$ | acceleration of gravity, |
| $P_0$ | 1000 mb, |
| $p$ | pressure, |
| $T$ | air temperature, and |
| $\rho$ | density. |

Equations (2) and (3) are forms of the tangential and radial equations of motion, respectively. Equation (4) is the first law of thermodynamics. Equation (6) is a simplified form of the continuity equation that can easily be justified on the basis of an order of magnitude analysis. Equation (5) is the hydrostatic equation.

Boundary conditions on the vertical motion at the top and bottom levels are

$$w_1=w_7=0, \tag{10}$$

where the subscript denotes level.

Equations (6) and (10) clearly filter the external gravity wave and thus allow larger time steps. However, as shown below, they place a restriction on the pressure field which must be retained in the numerical model for physical consistency. From (6) and (10),

$$\int_{z_1}^{z_7} \bar{\rho} u dz=0. \tag{11}$$

From (3) and (11),

$$\begin{aligned}\int_{z_1}^{z_7} \bar{\rho}\theta \frac{\partial \phi}{\partial r} dz=&\int_{z_1}^{z_7} \bar{\rho} \left\{\frac{M}{r}\left(f+\frac{M}{r^2}\right)-u\frac{\partial u}{\partial r}-w\frac{\partial u}{\partial z}\right\} dz\\ &+\int_{z_1}^{z_7} \bar{\rho}\left\{\frac{K_H}{r^2}\frac{\partial}{\partial r}\left[r^3\frac{\partial}{\partial r}\left(\frac{u}{r}\right)\right]\right.\\ &\left.+\frac{1}{\bar{\rho}}\frac{\partial}{\partial z}\left(\bar{\rho}K_z\frac{\partial u}{\partial z}\right)\right\} dz \\ \equiv& B.\end{aligned} \tag{12}$$

By use of the hydrostatic equation (5)

$$\int_{z_1}^{z_7} \bar{\rho}\theta \frac{\partial \phi}{\partial r} dz=\frac{\partial \phi_1}{\partial r}\int_{z_1}^{z_7} \bar{\rho}\theta dz-\int_{z_1}^{z_7} \bar{\rho}\theta\frac{\partial H}{\partial r} dz, \tag{13}$$

where

$$H=\int_{z_1}^{z}\frac{g}{\theta} dz' \tag{14}$$

and $z'$ is a dummy variable. From (12), (13), and (14),

$$\frac{\partial \phi_1}{\partial r}=\frac{B+\int_{z_1}^{z_7}\bar{\rho}\theta\frac{\partial H}{\partial r}dz}{\int_{z_1}^{z_7}\bar{\rho}\theta dz}. \tag{15}$$

Discarding viscous and diabatic effects, this system of equations with the boundary conditions (10) gives the energy integral

$$\frac{\partial}{\partial t}\int_0^{z_7}\int_0^{r^*}\bar{\rho}\left\{\frac{u^2+v^2}{2}+c_pT+gz\right\}rdrdz =\int_0^{z_7}\int_0^{r^*}\left(\frac{\bar{\rho}}{\rho}\right)\frac{\partial p}{\partial t}rdrdz, \tag{16}$$

provided that the domain is mechanically closed at $r=r^*$. If the complete form of the continuity equation,

$$\frac{\partial \rho}{\partial t}=-\frac{\partial \rho w}{\partial z}-\frac{1}{r}\frac{\partial(\rho r u)}{\partial r},$$

is used in place of (6), the energy integral analogous to (16) is

$$\frac{\partial}{\partial t}\int_0^{z_7}\int_0^{r^*}\rho\left(\frac{u^2v^2}{2}+c_pT+gz\right)rdrdz =\int_0^{z_7}\int_0^{r^*} r\frac{\partial p}{\partial t}drdz \tag{17}$$

which can be written in the more familiar form

$$\frac{\partial}{\partial t}\int_0^{z_7}\int_0^{r^*}\rho\left(\frac{u^2+v^2}{2}+c_vT+gz\right)rdrdz=0. \tag{18}$$

By comparison of (16) and (17), we see that the model is only approximate in its conservation of total energy.

The advection terms in (2), (3), (4), and (12) are calculated by the upstream noncentered method, and the time derivatives are calculated as forward differences. In the vertical, all variables are defined at all levels. Along the radius, a staggered grid is employed. $M$ and $u$ are defined at the grid points

$$r_j=(j-1)\Delta r,\ j=1,2,\ldots\ldots, \tag{19}$$

while $\theta$, $\phi$, $w$, and $\dot{Q}$ are given at

$$r_j=(j-\tfrac{1}{2})\Delta r,\ j=1,2,\ldots. \tag{20}$$

The mixing terms in (2), (3), (4), and (12) are evaluated by expressions similar to those previously used by the author (1964). To evaluate vertical mixing terms at levels 1 and 2, we invoke the boundary conditions

$$\left(\bar{\rho}K_z\frac{\partial M}{\partial z}\right)_{z_1}=C_D(\bar{\rho}_1|v_1|M_1) \tag{21}$$

and

$$\left(\bar{\rho}K_z\frac{\partial u}{\partial z}\right)_{z_1}=C_D(\bar{\rho}_1|v_1|u_1), \tag{22}$$

where $C_D$ is the (constant) drag coefficient, and $|v_1|$ is an approximation to $(u_1^2+v_1^2)^{1/2}$ made for computational economy.

The integrals required to calculate $w$ from (6) and $\phi$ from (5) are evaluated by the trapezoidal rule. The prognostic equations (2) and (3) are applied at the radial grid given by (19) and at vertical grid points for $i=1,2,\ldots,7$. At $j=1$ $(r=0)$,

$$M=0,\ u=0. \tag{23}$$

At $j=J_{max}$ $(r=440$ km$)$,

$$(ru)_{J_{max}}=(ru)_{J_{max}-1} \tag{24}$$

and

$$M_{J_{max}}=M_{J_{max}-1} \tag{25}$$

which are the conditions, respectively, that the horizontal divergence and relative vorticity vanish.

The potential temperature tendencies are evaluated on the radial grid defined by (20) and at vertical grid points for $i=3,4,\ldots,7$. The boundary condition at $J_{max}$ in the potential temperature forecast is

$$\theta_{J_{max}}=\theta_{J_{max}-1}. \tag{26}$$

The initial conditions consist of a weak vortex in gradient balance with no meridional circulation. This state of balance is achieved as follows. A field of standard potential temperature ($\bar{\theta}=\bar{\theta}(z)$) is specified. These values are very nearly those of the mean hurricane season sounding (Hebert and Jordan 1959) and are listed in table 2. The lower boundary condition $\bar{\phi}_1=c_p(1015/1000)^{R/c_p}$ is adopted, and a set of standard $\bar{\phi}=\bar{\phi}(z)$ are calculated from the hydrostatic equation (5). A set of standard temperatures ($\bar{T}=\bar{T}(z)$) are calculated from (8). Equation (7) is then used to calculate standard pressures ($\bar{p}=\bar{p}(z)$). Finally, the standard densities ($\bar{\rho}=\bar{\rho}(z)$) are obtained from $\bar{\rho}=\bar{p}/R\bar{T}$.

The initial temperature field is given by

$$T_{i,j}=\bar{T}_i+\epsilon\left\{\cos\frac{\pi}{\hat{r}}r_j+1\right\}\sin\frac{\pi}{z_7}z_i, \tag{27}$$

where $\epsilon=0.16$°K and $\hat{r}=(J_{max}-1)\Delta r$. With the boundary condition $\phi_{7,j}=\bar{\phi}_7$, the hydrostatic equation, in the form

$$\partial\phi/\partial z=-g\phi/c_pT, \tag{28}$$

is integrated by the trapezoidal rule to obtain $\phi_{i,j}$ for $i=6, 5, \ldots, 1$. With $T$ and $\phi$ initialized, initial values of $\theta$ are calculated from (8), the gradient wind equation is solved for the initial distribution of $v$, and $M$ is then calculated from (9).

The prognostic cycle proceeds as follows:

1) calculate $\dot{Q}$ by the method described in section 1,
2) forecast $M$ with equation (2),
3) calculate $\phi$ from (5) and (15),
4) forecast $u$ with (3),
5) calculate $w$ from (6),
6) forecast $\theta$ with (4), and
7) return to 1) above.

Dependent variables are replaced with their new values as soon as they become available. The scheme is, therefore, semi-implicit, and the results depend on the order in which the calculations are carried out. Indeed, computational stability is dependent on the order of the calculations. The sequence given above has proven to be highly stable.

After convection has been operative for some time, lapse rates become coincident with the reference pseudo-adiabat (Rosenthal 1969, fig. 8). In experiment I, the release of latent heat was terminated when this occurred. The so-called "large-scale" precipitation to be expected with macroscale ascent of statically stable, or neutral, saturated air was, therefore, neglected. The new experiments attempt to include this second source of latent heat by use of a technique employed in previous hurricane models (Yamasaki 1968).[1] Large-scale precipitation is activated only after convection has neutralized the conditional instability along a vertical. When the macroscale vertical motion is upward along such a vertical, the macroscale relative humidity is assumed to be 100 percent. Except for the effects of eddy diffusivity (which are ignored for this purpose), the macroscale motion must then be along a pseudoadiabat which coincides with the actual thermal stratification of the atmosphere, and, therefore, adiabatic cooling is exactly balanced by large-scale condensation; the temperature at a given point in space is, therefore, unaffected.

[1] A new series of experiments to be reported on in the near future includes an explicit prediction of specific humidity.

TABLE 2.—*Standard values of thermodynamic variables*

| Level | Height (m) | $\bar{\theta}$ (°K) | $\bar{T}$ 1(°K) | $\bar{p}$ (mb) | $\bar{\rho}$ (ton/m³) |
|---|---|---|---|---|---|
| 1 | 0 | 300 | 301.3 | 1015.0 | $1.174\times10^{-3}$ |
| 2 | 1,054 | 303 | 294.1 | 900.4 | $1.067\times10^{-3}$ |
| 3 | 3,187 | 313 | 282.6 | 699.4 | $0.862\times10^{-3}$ |
| 4 | 5,898 | 325 | 266.5 | 499.2 | $0.653\times10^{-3}$ |
| 5 | 9,697 | 340 | 240.8 | 299.2 | $0.433\times10^{-3}$ |
| 6 | 12,423 | 347 | 218.9 | 199.5 | $0.318\times10^{-3}$ |
| 7 | 16,621 | 391 | 203.1 | 101.1 | $0.173\times10^{-3}$ |

## 3. EXPERIMENTS D10 AND D20

The two new experiments are designated D10 and D20. Except for the release of latent heat by large-scale precipitation (see section 2), the physics of D10 and D20 are identical to experiment I; D10 and D20 differ from each other only in radial and temporal increments. Basic parameters for the three experiments are summarized in table 3. Strongest winds at the initial instant are about 7 m sec$^{-1}$ and are located at a radius of 250 km; the central pressure at this time is 1013 mb.

## 4. LIFE CYCLE AND STRUCTURE AT SEA LEVEL

The evolution of central pressure[2] and maximum surface wind for experiments I and D20 is shown in figure 1. We find differences only after 168 hr, when D20 is somewhat more intense. This difference is entirely due to the large-scale precipitation included in D20 but not in experiment I. Before 144 hr, precipitation in both experiments is entirely convective. Thereafter, D20 is supplied latent heat by both types of precipitation, whereas experiment I receives energy only through the convective release of latent heat. The latter process supplies energy in continually decreasing amounts as more of the storm is neutralized with respect to pseudo-adiabatic ascent (Rosenthal 1969, fig. 8).

The analogous data for experiment D10 are shown in figure 2. Differences between D10 and D20 are relatively minor. Peak intensity for D10 is reached about 24 hr

[2] Pressure is not defined at zero radius because of the grid staggering, equations (19) and (20). For experiments I and D20, central pressure is pressure $z=0$, $r=10$ km. For experiment D10, central pressure is that at $z=0$, $r=5$ km.

TABLE 3.—*Some experimental parameters*

| Parameter | Experiment I | Experiment D20 | Experiment D10 |
|---|---|---|---|
| Kinematic coefficient of eddy viscosity and/or eddy conductivity for lateral mixing | $10^4$ m² sec⁻¹ | same | same |
| Kinematic coefficient of eddy viscosity for vertical mixing | 10 m² sec⁻¹ at level 1; zero elsewhere | same | same |
| Drag coefficient | $3\times10^{-3}$ | same | same |
| Coriolis parameter | $5\times10^{-5}$ sec⁻¹ | same | same |
| Time increment | 120 sec | 120 sec | 60 sec |
| Radial increment | 20 km | 20 km | 10 km |
| Radial extent of computational domain | 440 km | same | same |
| Latent heat by large-scale precipitation | no | yes | yes |

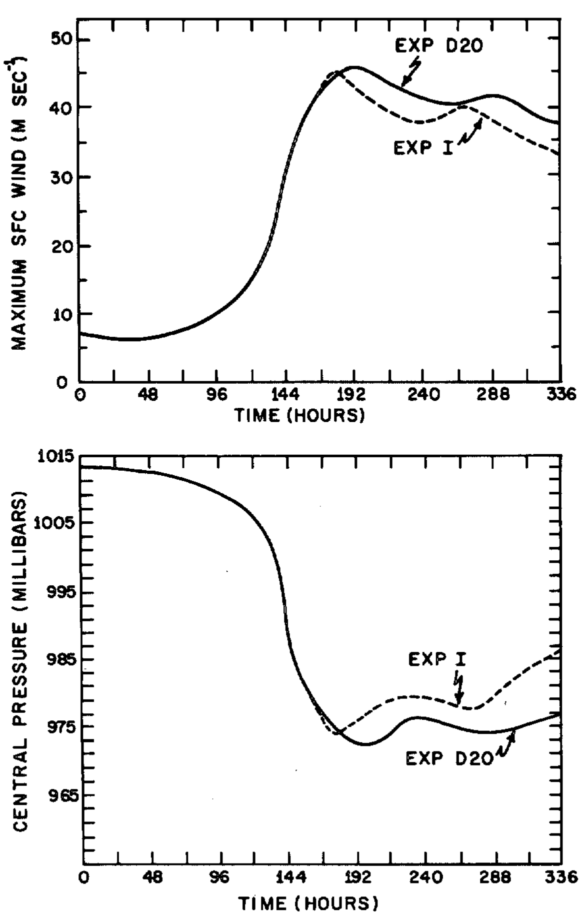


FIGURE 1.—Top, maximum surface wind as a function of time for experiments I and D20; bottom, central pressure as a function of time for experiments I and D20.

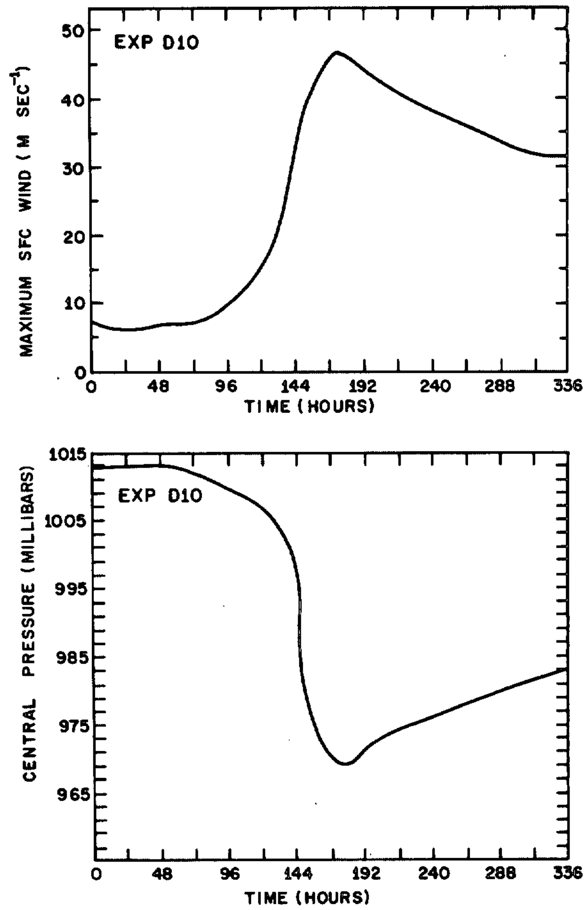


FIGURE 2.—Top, maximum surface wind as a function of time for experiment D10; bottom, central pressure as a function of time for experiment D10.

earlier than for D20. Also, D10 decays somewhat more rapidly than D20. At peak intensity, however, the maximum surface wind for D10 is only about 1 m sec$^{-1}$ greater than that for D20. Minimum central pressure for D10 is only 3.5 mb less than for D20.

On the basis of a recent calculation by Ooyama (1968), greater differences between D10 and D20 had been expected. Ooyama (1968) compared results of his model (Ooyama 1967) for different grid sizes with the numerical integration scheme used here. He found computational damping to decrease markedly as the radial resolution was refined. Significantly stronger winds and deeper central pressure were found with the smaller grid increments. Such a result is generally to be expected with upstream differencing (Molenkamp 1968*a*). The rather minor differences between D10 and D20 were, therefore, surprising.

Figure 3 shows that D20 gives a larger storm with a substantially longer period of hurricane-force winds. In experiment D10, the strongest winds and vertical motions occur closer to the storm center than is the case for D20. In general, such a result should be anticipated with more closely spaced grid points. However, part of the explanation is fairly subtle. Ooyama's (1967) study as well as a series of experiments with our model (section 9) indicate maximum winds and vertical motions occur closer to the storm center when smaller lateral mixing coefficients are used. Although the explicit coefficient of lateral mixing is identical for D10 and D20, these calculations contain a

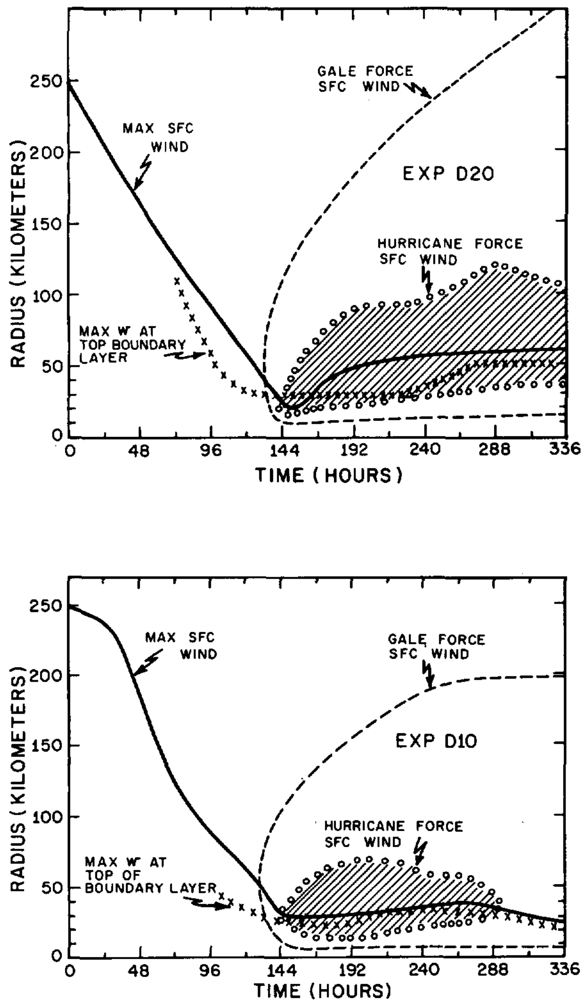


Figure 3.—Radii of maximum surface wind and maximum vertical motion at the 1054-m level; outer and inner limits of gale- and hurricane-force winds at the surface. Top, experiment D20; bottom, experiment D10.

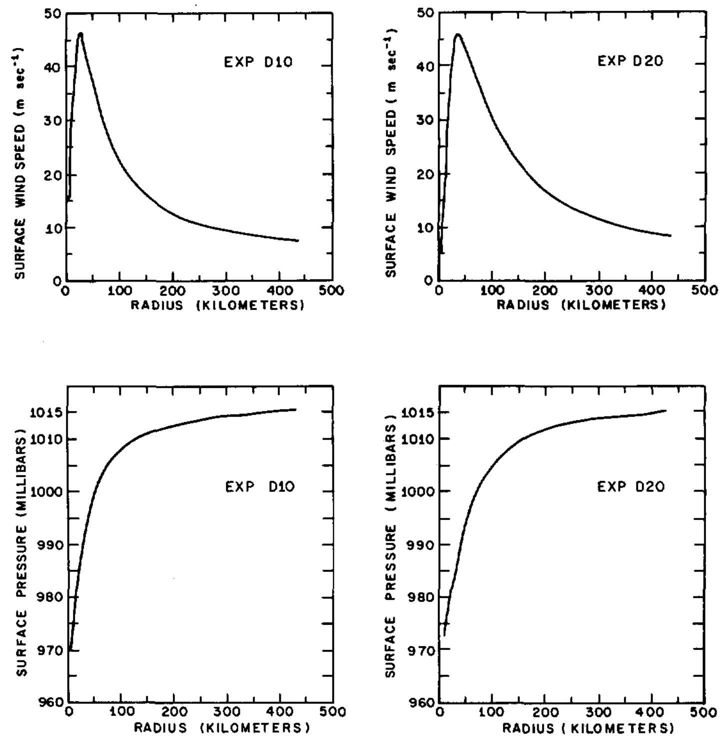


Figure 4.—Radial profiles of surface wind speed and surface pressure. Left, experiment D10 at 168 hr; right, experiment D20 at 192 hr.

computational lateral mixing that is produced by upstream differencing of advection terms (section 9). The implicit or computational lateral mixing is proportional to the grid increment and, hence, is smaller in experiment D10. From figure 3 we also find that the region covered by winds in excess of gales continually expands in experiment D20; whereas in experiment D10, gale-force winds are constrained to lie within 200 km of the storm center.

One final aspect of figure 3 should be noted. In both experiments, the largest boundary-layer vertical motion occurs inside the maximum-surface wind. This is in contrast to Ooyama's (1967) results and is explicable (Ooyama 1968) by his use of the gradient-wind assumption in the boundary layer.

Radial profiles of surface wind and surface pressure at the time of deepest central pressure are shown in figure 4. The profiles for both experiments are quite realistic; however, as already indicated by figure 3, D10 yields a much more compact storm with greater concentration of wind speed and pressure deficit in the inner core.

## 5. VERTICAL CROSS-SECTIONS

Figures 5 through 8 compare vertical cross-sections of tangential wind, temperature anomaly, radial wind, and vertical motion for experiments D10 and D20. As before, the data are appropriate to the time of deepest central pressure. Both experiments provide quite realistic storm structure (compare with empirical results of, for example, Hawkins and Rubsam 1968).

A number of important, if subtle, improvements in structure are, however, found in D10. In figure 6, we note that between radii of 50 and 150 km, D20 yields greatest temperature anomaly at 500 mb. This somewhat unrealistic feature was also found in experiment I (Rosenthal 1969) and is substantially improved in D10.

The results of experiment I (Rosenthal 1969) showed maximum outflow at the 100-mb level, and from figure 7 we see that this is also the case with D20. On the other hand, D10 shows an outflow pattern more consistent with ideas of previous writers (see, for example, Hawkins and Rubsam 1968).

Experiment I showed 20-km resolution to be insufficient for resolving the eye dynamics. As a result, subsidence at the storm center was not a permanent feature of a mature stage but rather a feature that appeared, dissappeared, and reappeared (Rosenthal 1969). A similar result is found for experiment D20, as is verified by inspecting figure 8. Experiment D10, on the other hand, shows a distinct region of subsidence at the storm center, and this persists throughout the mature stage.

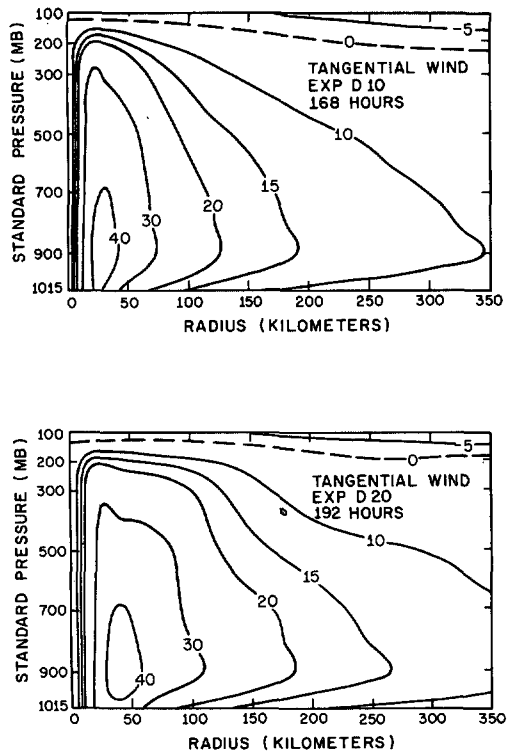


FIGURE 5.—Vertical cross-sections of tangential wind; top, experiment D10 at 168 hr; bottom, experiment D20 at 192 hr. Isopleths are labeled in m $sec^{-1}$. Positive values are cyclonic winds.

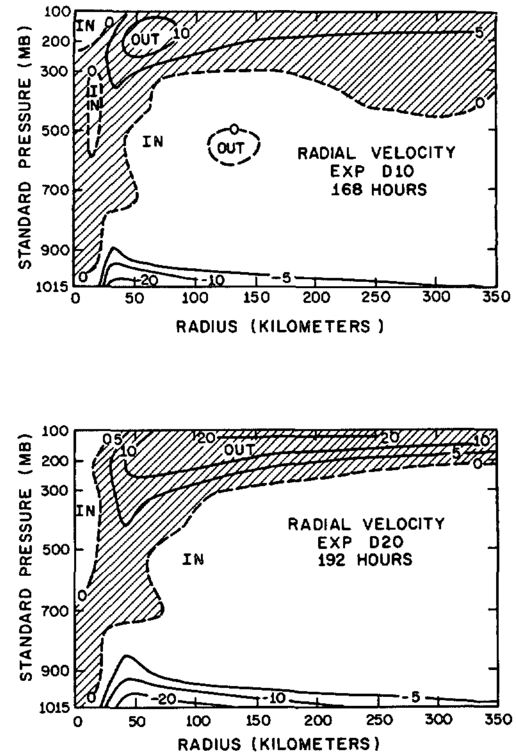


FIGURE 7.—Vertical cross-sections of radial wind; top, experiment D10 at 168 hr; bottom, experiment D20 at 192 hr. Isopleths are labeled in m $sec^{-1}$.

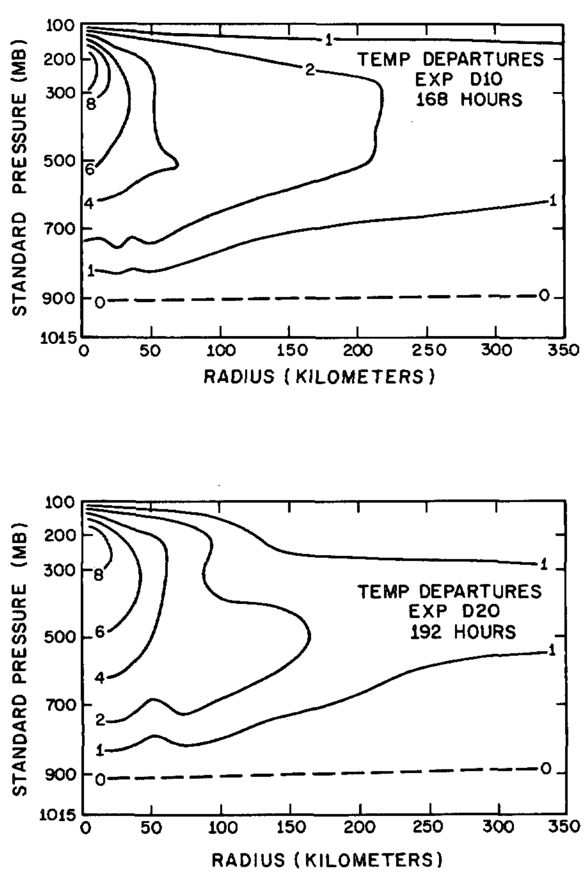


FIGURE 6.—Vertical cross-sections of temperature excess over the mean tropical atmosphere; top, experiment D10 at 168 hr; bottom, experiment D20 at 192 hr. Isopleths are labeled in °K.

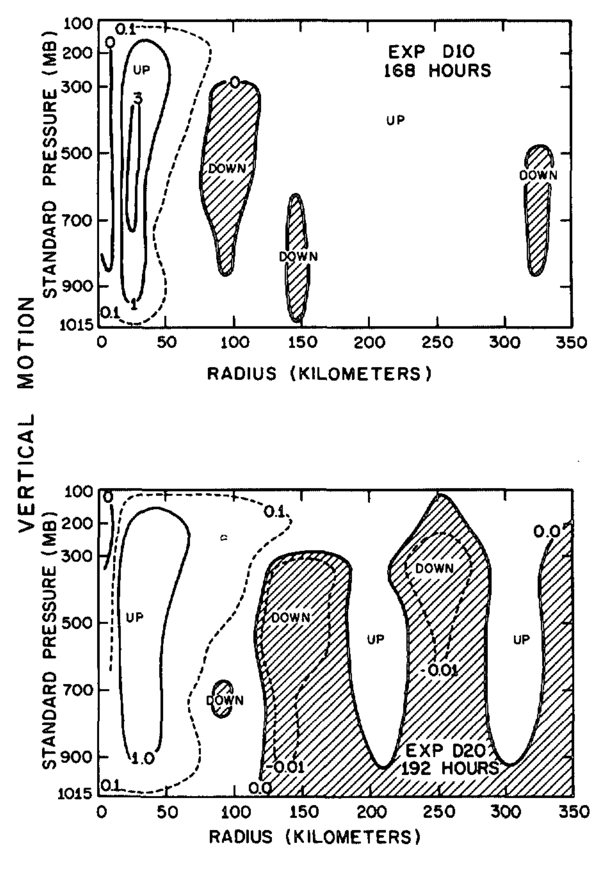


FIGURE 8.—Vertical cross-sections of vertical velocity; top, experiment D10 at 168 hr. Isopleths are drawn at variable intervals and labeled in m $sec^{-1}$; bottom, experiment D20 at 192 hr.

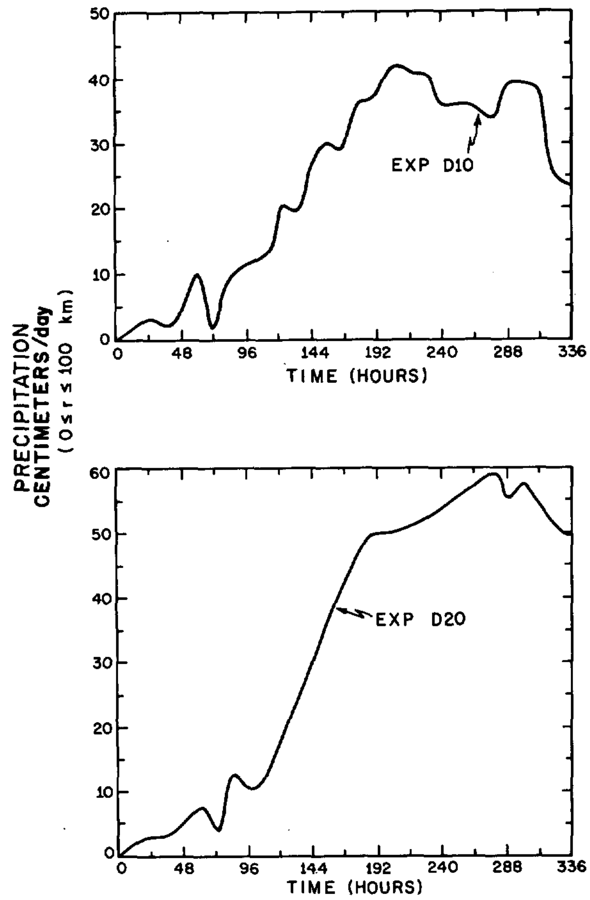


FIGURE 9.—Average precipitation over the radial interval zero to 100 km. Precipitation values are sums of the convective and large-scale rainfall rates; top, experiment D10; bottom, experiment D20.

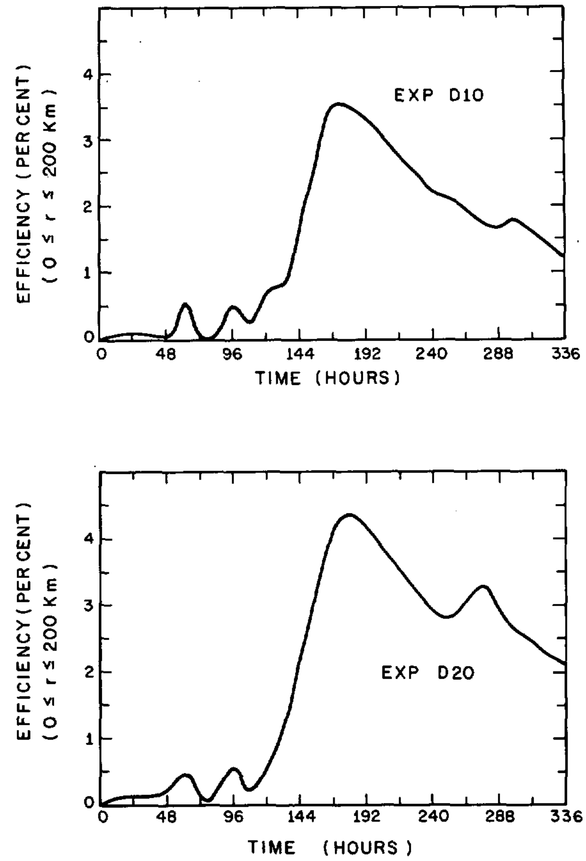


FIGURE 11.—Efficiency of the tropical cyclone. Efficiency is defined as the ratio of the rate of kinetic energy production to the rate of condensation heating. Condensation heating includes both the convective and the large-scale contributions. Values plotted are averages over the radial interval zero to 200 km. Top, experiment D10; bottom, experiment D20.

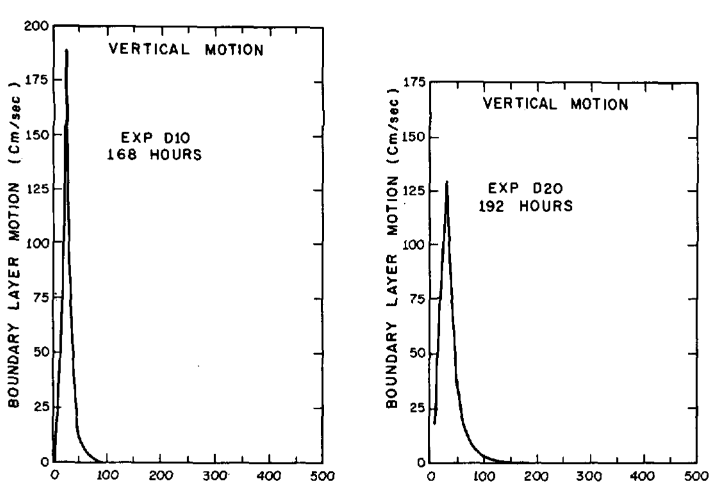


FIGURE 10.—Radial profiles of the vertical velocity at level 2; left, experiment D10 at 168 hr; right, experiment D20 at 192 hr.

## 6. PRECIPITATION AND EFFICIENCY

Rainfall rates, averaged over the inner 100 km, are shown in figure 9. Experiments D10 and D20 both give fairly reasonable, if somewhat large values [3] of precipitation. Rainfall is somewhat less in D10. In neither experiment does large-scale precipitation appear before the 144th hour. Comparison of the convective and large-scale rainfall rates (figure not shown) shows that by the end of the calculation the rainfall in the inner 100 km of D10 is entirely large-scale; the thermal structure there has been neutralized and pseudoadiabatic lapse rates prevail. For experiment D20, on the other hand, large-scale precipitation is never found beyond the inner 60 km.

The main controlling factor for the convective rainfall is the vertical motion at level 2. Figure 10 shows radial profiles of this quantity at the times of deepest central pressure. The maximum vertical motion for D10 is about 40 percent greater than for D20. Because of the difference in resolution, D20 builds a broader "eye wall" and the average vertical motion over the inner 100 km is larger for D20. This explains the larger average rainfall rate (fig. 9) for D20.

The "efficiency" of a tropical cyclone is usually defined as the ratio of kinetic energy production to latent heat release. Figure 11 shows average values of

[3] The tendency for the rainfall to be on the heavy side was also found in experiment I. This appears to be directly attributable to the absence of a mechanism for atmospheric storage of water vapor. Newer experiments (see footnote 1) remedy this situation.

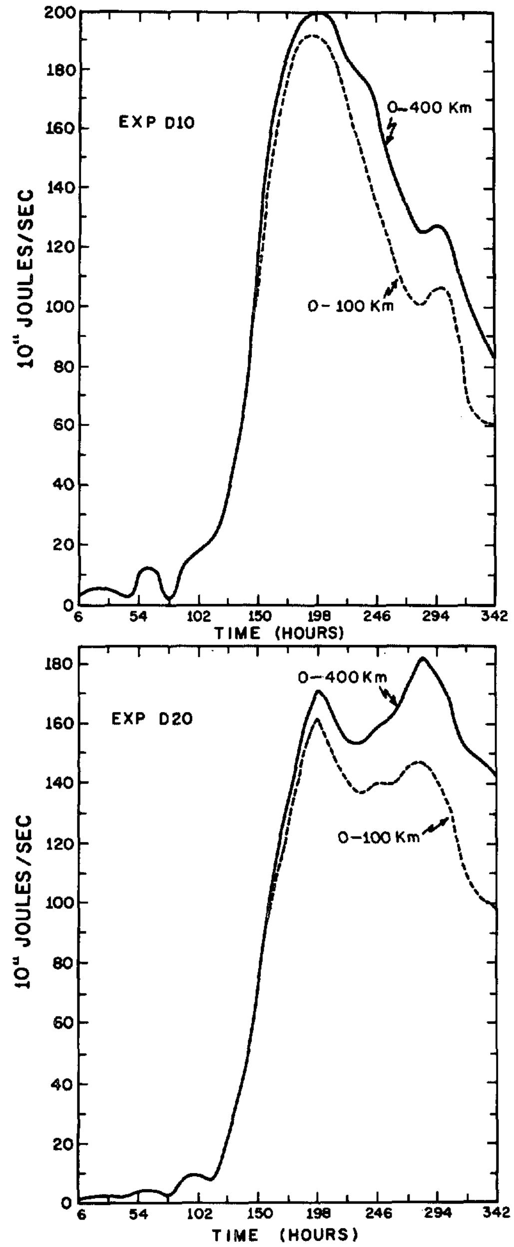


FIGURE 12.—Generation of available potential energy by condensation heating (total of convective and large-scale releases of latent heat). Solid lines represent totals for the radial interval zero to 400 km. Dashed lines give contributions for the radial interval zero to 100 km.

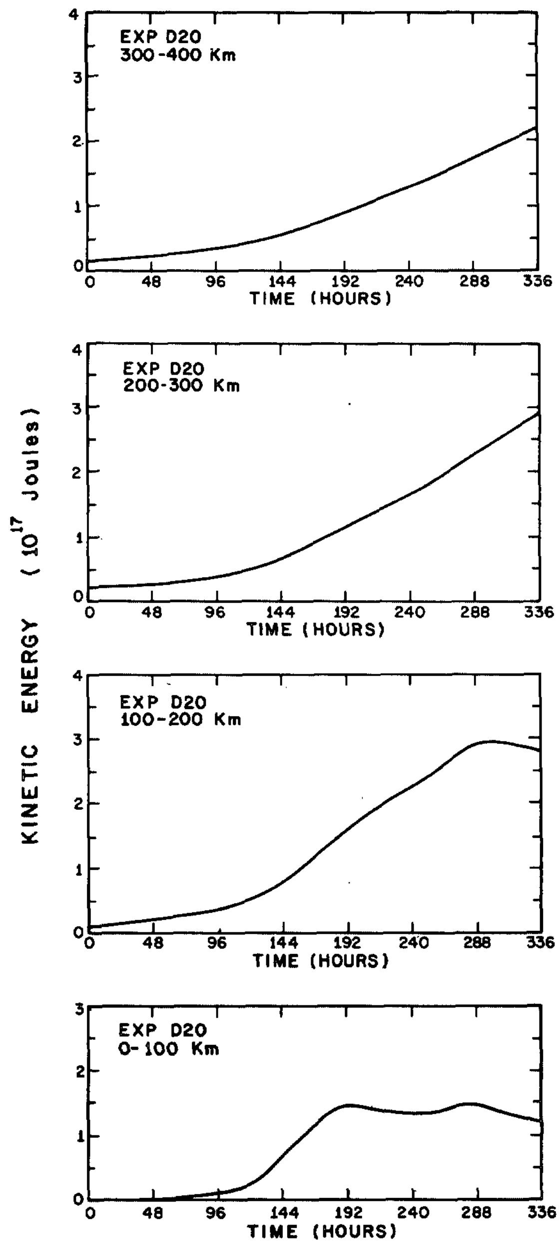


FIGURE 13.—Variation with time of the kinetic energy content of various rings of the storm for experiment D20.

these efficiencies for the inner 200 km of the two experiments. Both experiments give reasonable values (Ooyama 1968, Palmén and Riehl 1957), but those for D20 are somewhat larger.

## 7. GENERATION OF AVAILABLE POTENTIAL ENERGY

The generation of available potential energy [4] by the total release of latent heat (convective plus large-scale) is shown in figure 12. During the earlier phases of the experiments, the generation rates for D10 are significantly greater than those for D20. This is in contrast to the total release of latent heat which, as we have already seen, is larger for D20.

In both experiments, generation during the first 200 hr or so is largely limited to the inner 100 km. Only late in the life cycle do the remaining portions of the circulation become active as generators of available potential energy. Even then, however, generation in the outer 300 km is quite small in D10. Experiment D20, on the other hand, generates substantial available potential energy in the 100- to 400-km ring.

Compared with empirical data (Anthes and Johnson 1968), the generation rates for both experiments are of the correct order of magnitude but somewhat too large. This is probably related to the excessive rainfall rates discussed in section 6.

[4] The computational method is described in the appendix.

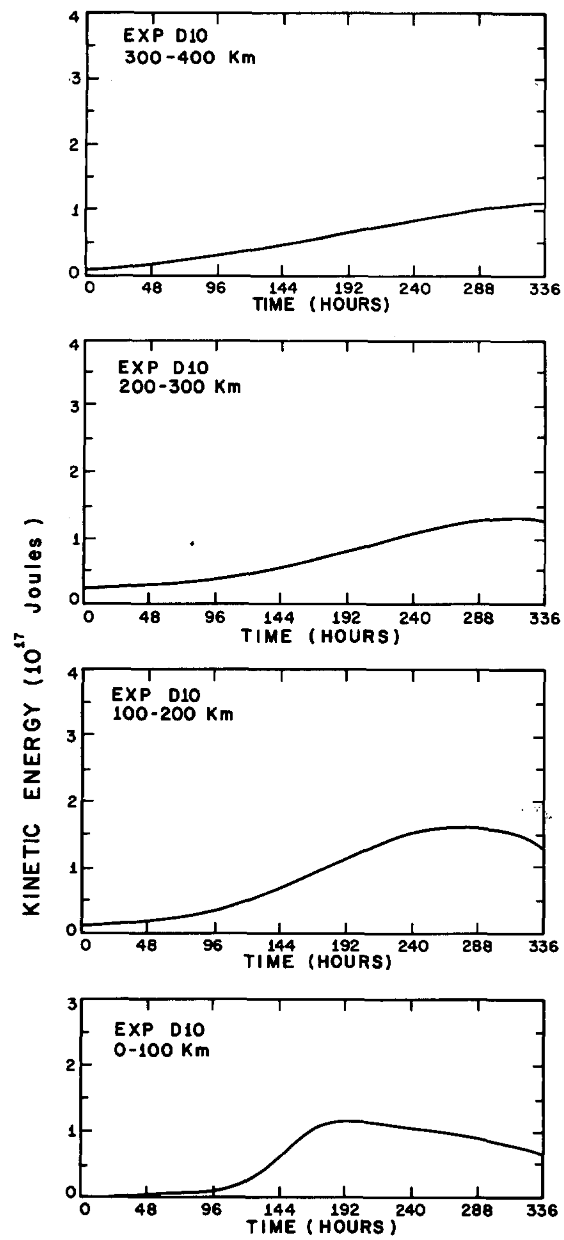


FIGURE 14.—Variation with time of the kinetic energy content of various rings of the storm for experiment D10.

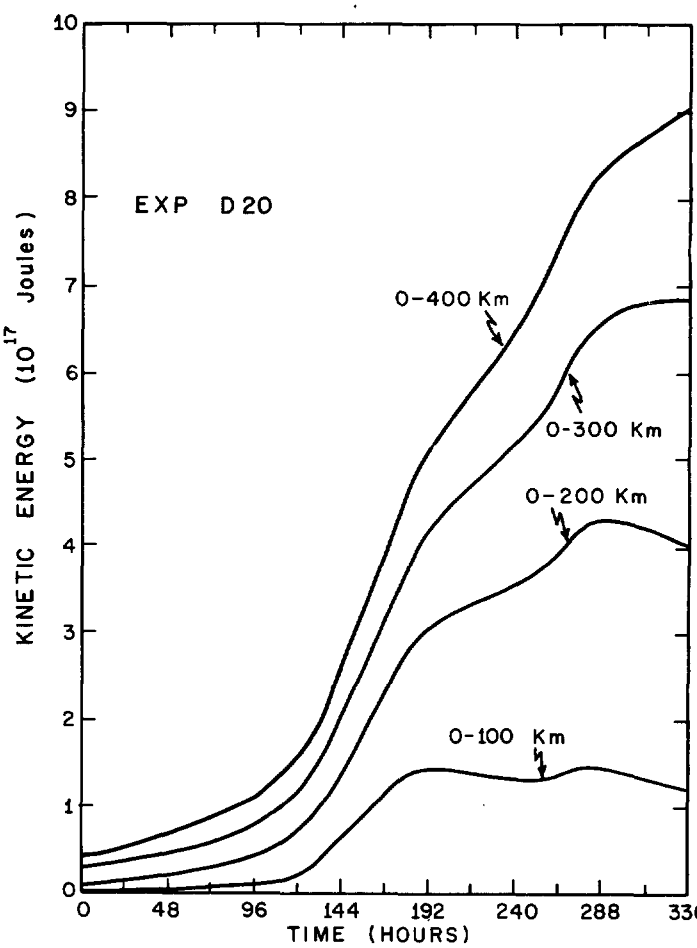


FIGURE 15.—Variation with time of the kinetic energy content of various radial intervals for experiment D20.

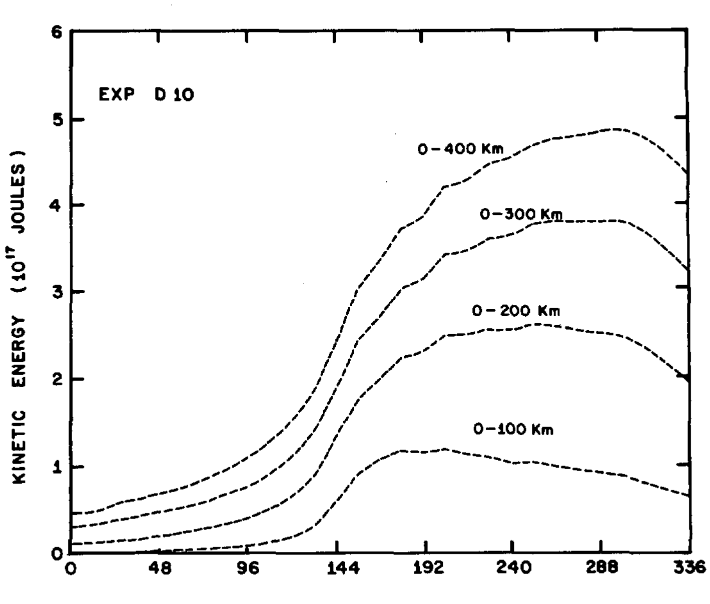


FIGURE 16.—Variation with time of the kinetic energy content of various radial intervals for experiment D10.

## 8. KINETIC ENERGY BUDGETS

Figures 13 and 14 show that reasonable agreement between the kinetic energies of the two experiments is achieved only in the inner 100 km. In the outer rings, the kinetic energy content of D20 is two to three times greater than that of D10. In the 200- to 300-km and 300- to 400-km rings, kinetic energy increases throughout the history of D20. In D10, on the other hand, maxima of kinetic energy are reached near the end of the calculation. In D10, the storm as a whole (0 to 400 km) has clearly passed its maximum of kinetic energy by the end of the computation, but in D20 the kinetic energy is increasing even at this time (figs. 15 and 16).

Components of the kinetic energy budgets (see footnote 4) are shown by figures 17 and 18. Except for the lateral

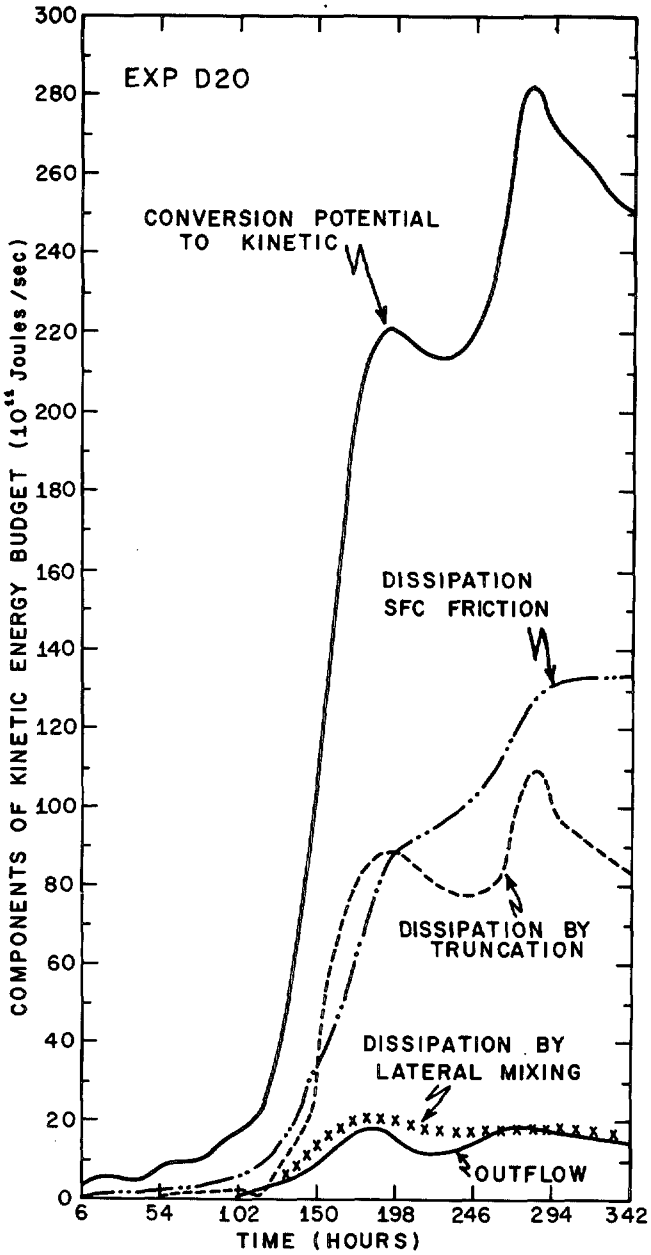


FIGURE 17.—Experiment D20 components of the kinetic energy budget as a function of time. Values are appropriate to the radial interval from zero to 400 km and are 12-hr averages.

mixing term, the components of the D20 budget are each substantially greater than their counterparts in D10. During most of both experiments, the only positive contribution to the kinetic energy tendency is the generation term. The only possible explanation for the higher kinetic energy content of D20 is that, in comparison to D10, it overestimates generation.

## 9. LATERAL MIXING AND PSEUDO-VISCOSITY

Figure 19 compares the results of a series of experiments (20-km resolution) in which the lateral mixing coefficient was varied. In view of the rather minor contribution to the kinetic energy budget (fig. 17) made by lateral mixing, the differences between the results with $K_H=10^4$ m$^2$ sec$^{-1}$ and $10^3$ m$^2$ sec$^{-1}$ (fig. 19) are at first surprising.

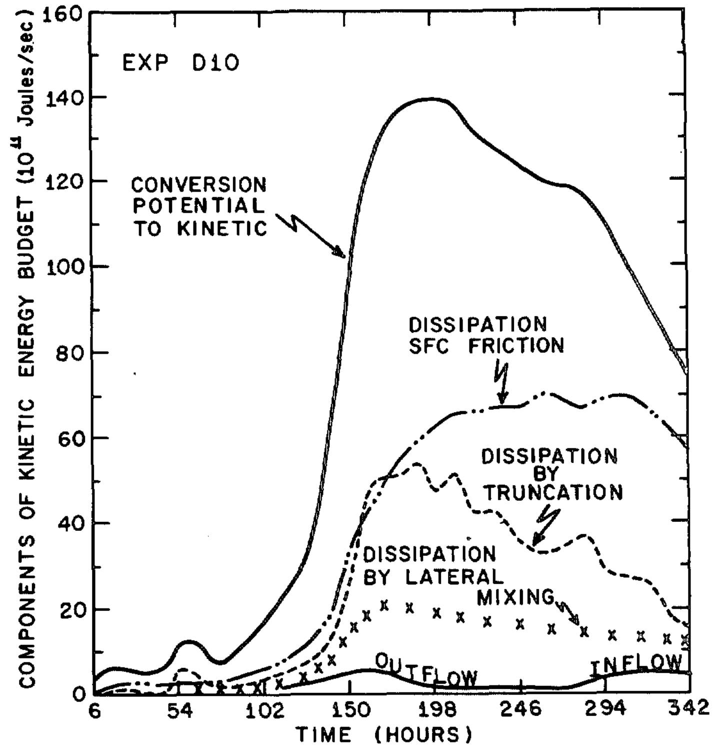


FIGURE 18.—Same as figure 17 but for experiment D10.

By comparison of figures 17 and 20, however, it becomes clear that the dissipation by lateral mixing is of the same order of magnitude as the time rate of change of kinetic energy. The differences in the experimental results when $K_H$ is reduced from $10^4$ to $10^3$ m$^2$ sec$^{-1}$ are, therefore, understandable. On the other hand, figure 19 also shows that further reduction of $K_H$ from $10^3$ m$^2$ sec$^{-1}$ to zero has rather little effect. This can be explained on the basis of the computational damping.

Consider the simple advection equation

$$\frac{\partial A}{\partial t}=-V\left(\frac{\partial A}{\partial s}\right) \tag{29}$$

and the finite-difference analog attained with upstream space and forward time differences,

$$A_j^{\tau+1}-A_j^{\tau}=-\frac{V(A_j^{\tau}-A_{j-1}^{\tau})\Delta t}{\Delta s} \tag{30}$$

where $V$ is presumed to be positive and constant. It may be shown (Molenkamp 1968$a$)[5] that the solutions of (4) approximate those of

$$\frac{\partial A}{\partial t}=-V\frac{\partial A}{\partial s}+\nu\frac{\partial^2 A}{\partial s^2}, \tag{31}$$

where the pseudoviscosity coefficient ($\nu$) is given by

$$\nu=\frac{1}{2}|V|\left\{1-\frac{|v|\Delta t}{\Delta s}\right\}\Delta s. \tag{32}$$

[5] Molenkamp obtains equations (31) and (32) by replacing the finite differences in (30) with differential expressions obtained from second-order power series expansions of $A$ in time and space and by use of (29). A more exact expression for $\nu$ may be found by equating the exact solution of (30) to the solution of $\partial A/\partial t=-u^*\partial A/\partial s+\nu\partial^2A/\partial s^2$. This yields two equations that can be solved for $u^*$ and $\nu$. It may further be shown that (32) is an approximation to the $\nu$ calculated by the method described in this footnote.

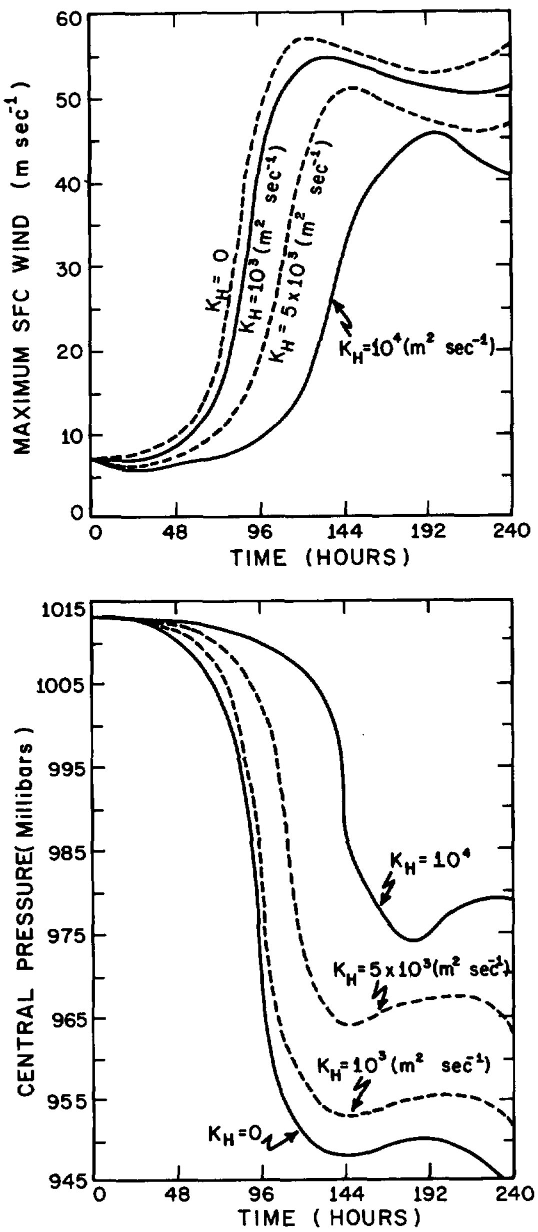


FIGURE 19.—Top, maximum surface wind as a function of time for a series of experiments in which the lateral mixing coefficient is varied, radial resolution is 20 km; bottom, central pressure as a function of time for the same series of experiments.

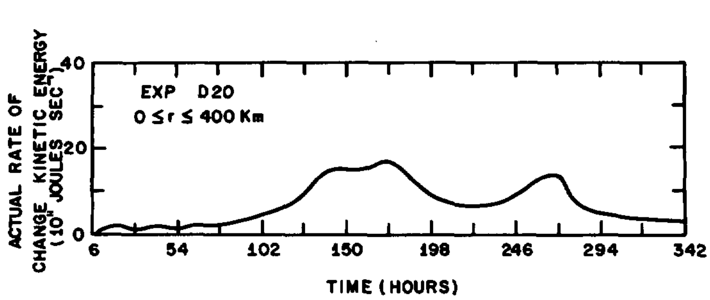


FIGURE 20.—Actual time rate of change of kinetic energy in the radial interval zero to 400 km for experiment D20. Differences are taken over 12 hr and calculations were made every 12 hr.

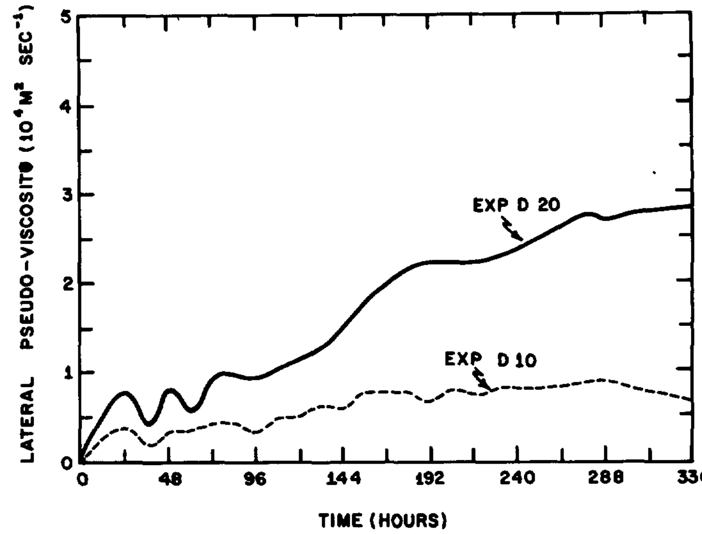


FIGURE 21.—Variation with time of the mass-averaged lateral pseudoviscosity for experiments D10 and D20. Averages are taken over the radial interval zero to 400 km and from level 1 to level 7.

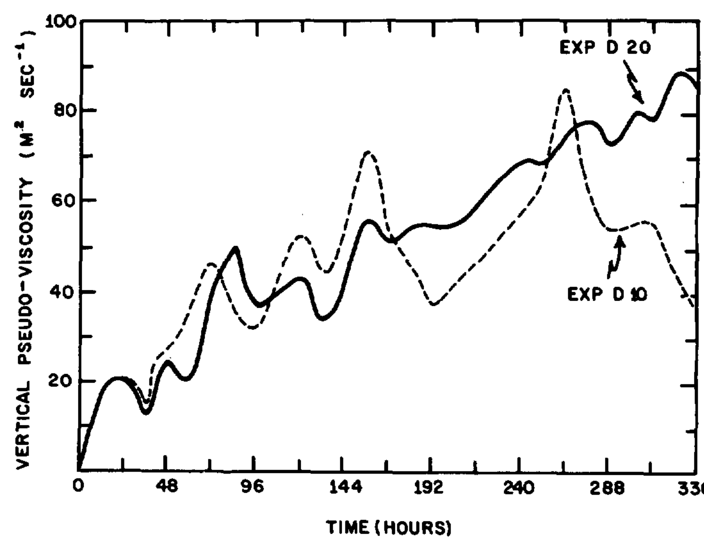


FIGURE 22.—Same as figure 21 but for the vertical pseudoviscosity.

By use of equation (32), the pseudoviscosity coefficients for both lateral and vertical mixing were computed for experiments D10 and D20. Those for lateral mixing, mass averaged over the entire storm, are given in figure 21, which shows the pseudoviscosity for lateral mixing to be on the order of $10^4$ m$^2$ sec$^{-1}$. Since this is also the order of the explicit lateral mixing coefficient, reduction of $K_H$ from $10^4$ to $10^3$ m$^2$ sec$^{-1}$ produces a substantial reduction in the total effective lateral dissipation. On the other hand, when the explicit lateral viscosity is $10^3$ m$^2$ sec$^{-1}$, the total effective lateral dissipation is already dominated by the pseudoviscosity; further reduction of $K_H$ therefore has a negligible effect on the total effective lateral mixing. A similar effect in Ogura's (1963) convection experiments is discussed by Molenkamp (1968*a*).

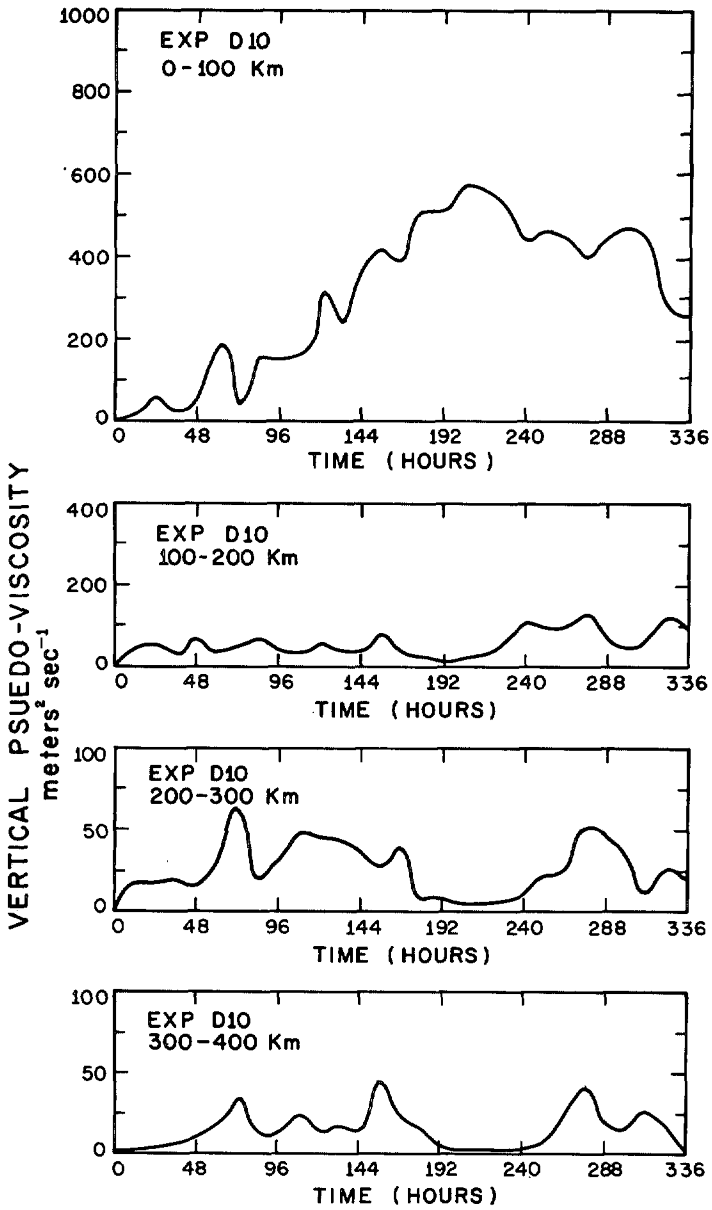


Figure 23.—Variation with time of mass-averaged vertical pseudoviscosity for various rings of the storm for experiment D10.

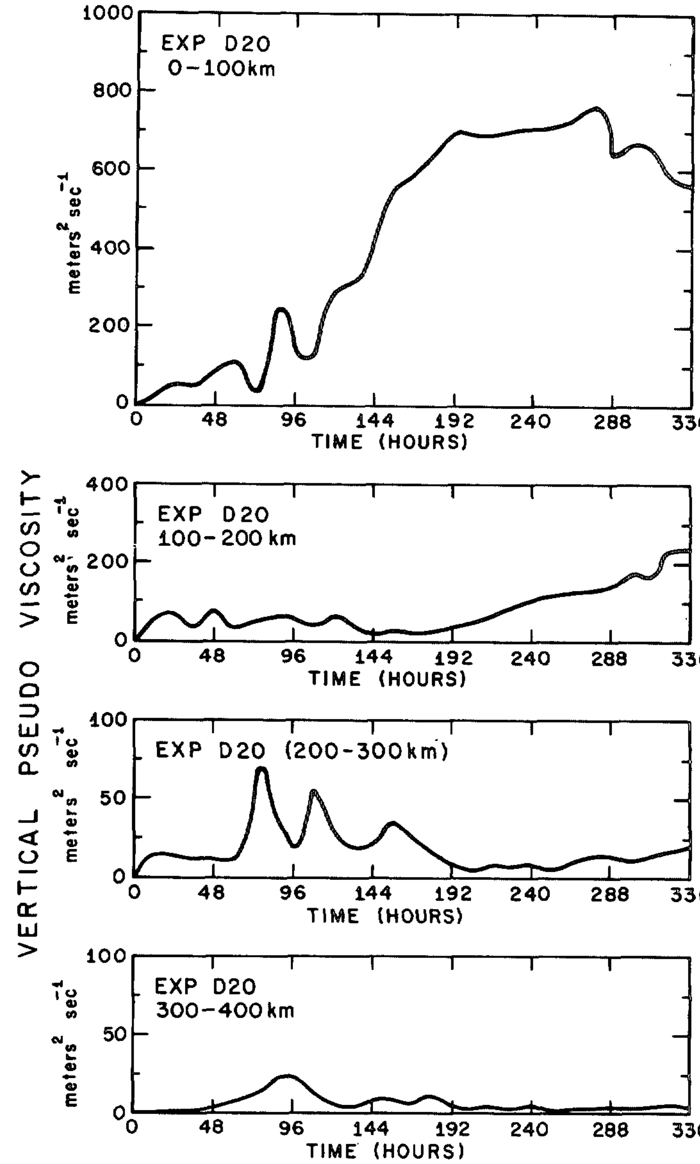


Figure 24.—Same as figure 23 but for experiment D20.

As noted in section 2, explicit internal vertical mixing was not included because the numerical damping was believed to provide sufficient internal dissipation. In experiment I (Rosenthal 1969), it was found that the sum of the computational damping and explicit lateral mixing gave a total effective internal dissipation comparable to that produced by drag friction. This rough one-to-one relationship between internal and surface dissipation is about that found for some real storms (Miller 1962, Riehl and Malkus 1961) and therefore provides some justification for omission of the explicit vertical viscosity.

Additional information on this matter is given in figure 22, which shows the pseudoviscosity coefficients for vertical mixing averaged over the entire storm. Compared with explicit eddy viscosities suggested by previous hurricane investigators (for example, Ooyama 1967, Kasahara 1961), the pseudoviscosities are quite large. Vertical averages for individual 100-km rings are shown in figures 23 and 24. The magnitudes are startling, especially in the inner 100 km where the coefficients approach $10^3$ m$^2$ sec$^{-1}$.

Since the results of experiments I, D20, and D10 are all fairly realistic, it seems reasonable to conclude that a model written in a nondissipative finite-difference scheme would require explicit dissipation coefficients substantially larger than those that have been used before.

## 10. SUMMARY AND DISCUSSION

Reduction of the radial increment from 20 to 10 km improves some aspects of the storm structure. Most noteworthy is the appearance of a distinct region of subsidence at the center, which is analogous to the eye of a real hurricane. With 20-km resolution, the size of the storm (measured by the area covered by winds exceeding gale force) continually increases with time. In the 10-km case, this region is contained within a radius of 200 km of the storm center.

In comparison to 10-km resolution, 20-km resolution tends to overestimate rainfall, efficiency, and kinetic energy production; generation of available potential energy is underestimated. While computational damping due to upstream differencing of the advection terms is substantially greater with 20-km resolution, the deepest central pressure and the strongest surface winds are almost the same for the two experiments. The kinetic energy budgets for the two experiments show the 20-km experiment to have substantially greater kinetic energy and kinetic energy generation.

The rainfall rates in both experiments are reasonable but somewhat heavy. This is attributable to the lack of a water vapor storage mechanism, which in turn, is related to the absence of an explicit forecast of specific humidity. This deficiency has already been corrected, and the results of a new series of experiments will be reported in the near future.

As a measure of the computational damping produced by upstream differencing, the pseudoviscosity coefficients derived by Molenkamp (1968*a*) were presented. Averaged over the entire storm, the values for lateral mixing in both experiments were on the order of $10^4$ m$^2$ sec$^{-1}$. The values with 20-km resolution were two to three times larger than those found with 10-km resolution. In both experiments the lateral pseudoviscosity was of the same order of magnitude as the explicit lateral mixing.

For vertical mixing, the pseudoviscosity coefficients were quite large compared with eddy viscosities generally accepted to be valid for hurricanes. Averaged over the storm as a whole, these pseudoviscosities were 40 to 80 m$^2$ sec$^{-1}$. When averaged only over the inner 100 km, values on the order of 200 to 800 m$^2$ sec$^{-1}$ were obtained. This is over an order of magnitude greater than explicit eddy viscosities suggested earlier by hurricane modelers.

In both experiments, the total internal dissipation (sum of the explicit lateral viscosity, the vertical pseudoviscosity, and the lateral pseudoviscosity) of kinetic energy is roughly comparable to the dissipation at the lower boundary by drag friction. A rough equivalence between internal and external dissipation is also found in empirical studies. This, together with the fact that the major part of the internal dissipation is computational rather than explicit, leads to the conclusion that if the model were to be expressed in a nondissipative numerical system, extremely large explicit lateral and vertical viscosities would be required to obtain reasonable results.

As pointed out before (Rosenthal 1969), upstream differencing for this model is dictated by economic considerations. Despite the undesirable aspects of this numerical system, it has yielded important results for a number of meteorological problems (examples are Ogura 1963, Orville 1964). For this reason, the rather strong condemnations of this method that have appeared in recent literature (Molenkamp 1968*a*, 1968*b*) cannot be entirely accepted. The major criticism appears to be the computational damping discussed above. It has been pointed out (Lilly 1961) that the damping provided by upstream differencing is effective in the suppression of nonlinear computational instability and that its general behavior is similar to that of the explicit nonlinear eddy viscosity used through the years by Smagorinsky and his group (Smagorinsky 1963).

## APPENDIX

By use of equations (2), (3), (6), (9), and (10), we may derive the following expression for the kinetic energy tendency of the storm:

$$\frac{\partial K}{\partial t}=T_E+I-D_V-D_H, \tag{33}$$

where

$$K=2\pi\int_0^{r_b}\int_{z_1}^{z_7}\frac{\bar{\rho}r(u^2+v^2)}{2}\,dz\,dr, \tag{34}$$

$$T_E=-2\pi\int_0^{r_b}\int_{z_1}^{z_7}\bar{\rho}ru\theta\frac{\partial\phi}{\partial r}\,dz\,dr, \tag{35}$$

$$I=-2\pi\int_{z_1}^{z_7}\bar{\rho}r_bu_b\left(\frac{u_b^2+v_b^2}{2}\right)dz, \tag{36}$$

$$D_V=-2\pi\int_0^{r_b}\int_{z_1}^{z_7}r\left\{u\frac{\partial}{\partial z}\left(\bar{\rho}K_z\frac{\partial u}{\partial z}\right)+v\frac{\partial}{\partial z}\left(\bar{\rho}K_z\frac{\partial v}{\partial z}\right)\right\}dz\,dr, \tag{37}$$

and

$$D_H=-2\pi K_H\int_0^{r_b}\int_{z_1}^{z_7}\frac{\bar{\rho}}{r}\left\{u\frac{\partial}{\partial r}\left[r^3\frac{\partial}{\partial r}\left(\frac{u}{r}\right)\right]+v\frac{\partial}{\partial r}\left[r^3\frac{\partial}{\partial r}\left(\frac{v}{r}\right)\right]\right\}dz\,dr. \tag{38}$$

To evaluate the vertical mixing terms, we invoke the boundary conditions (21) and (22). With the distribution of $K_z$ used for these experiments (table 3) and from (21) and (22), we have

$$D_V\approx2\pi\int_0^{r_b}r\bar{\rho}_1C_D|v_1|(u_1^2+v_1^2)dr. \tag{39}$$

For the sake of brevity, the dissipation produced by lateral eddy viscosity is written in the form of equation (38), rather than in a form that separates internal dissipation from dissipation at the lateral boundary.

If we average equation (33) over a time interval $\tau$, we obtain

$$\frac{\partial\tilde{K}}{\partial t}=\frac{K^{(t+\tau)}-K^{(t)}}{\tau}=\tilde{T}_E+\tilde{I}-\tilde{D}_V-\tilde{D}_H, \tag{40}$$

where

$$\tilde{(\ )}=\frac{1}{\tau}\int_t^{t+\tau}(\ )dt'. \tag{41}$$

All terms of equation (40) may be evaluated directly from the output of the model. In general, there will be a significant imbalance because of truncation error. The kinetic energy budgets shown in figures 17 and 18 of the text are based on 12-hr averages with computations at 12-hr intervals.

The generation of available potential energy was calculated from the approximate relationship

$$G=\frac{2\pi g^2}{c_p}\int_0^{r_b}\int_{z_1}^{z_2}\frac{\overline{T'S'}}{\overline{T}^2\overline{N}^2}\bar{\rho}r\,dr\,dz, \tag{42}$$

where

$$\overline{(\ )}=\frac{2\pi\int_0^{r^*}(\ )r\,dr}{\pi r^{*2}}, \tag{43}$$

$$r^*=400\ km, \tag{44}$$

$$(\ )'=(\ )-\overline{(\ )}, \tag{45}$$

$$N^2=\left(\frac{g}{\theta}\right)\left(\frac{\partial\theta}{\partial z}\right), \tag{46}$$

and $S$ is the total (convective plus large-scale) condensation heating per unit time and mass.

## ACKNOWLEDGMENTS

We are indebted to Mr. James W. Trout who provided substantial assistance with many of the calculations discussed above.

## REFERENCES

Anthes, Richard A., and Johnson, Donald R., "Generation of Available Potential Energy in Hurricane Hilda (1964)," *Monthly Weather Review*, Vol. 96, No. 5, May **1968**, pp. 291–302.

Charney, Jule G., and Eliassen, Arnt, "On the Growth of the Hurricane Depression," *Journal of the Atmospheric Sciences*, Vol. 21, No. 1, Jan. **1964**, pp. 68–75.

Garstang, Michael, LaSeur, Noel E., and Aspliden, Carl, "Equivalent Potential Temperature as a Measure of the Structure of the Tropical Atmosphere," *Final Report* No. 67-10, Contract No. DA-AMC-28-043-66-G25, Florida State University, Tallahassee, Aug. **1967**, 44 pp.

Gray, William M., "Global View of the Origin of Tropical Disturbances and Storms," *Atmospheric Science Papers* No. 114, Department of Atmospheric Science, Colorado State University, Fort Collins, Oct. **1967**, 105 pp.

Hawkins, Harry F., and Rubsam, Daryl T., "Hurricane Hilda, 1964: II. Structure and Budgets of the Hurricane on October 1, 1964," *Monthly Weather Review*, Vol. 96, No. 9, Sept. **1968**, pp. 617–636.

Hebert, Paul J., and Jordan, C. L., "Mean Soundings for the Gulf of Mexico Area," *National Hurricane Research Project Report* No. 30, U.S. Weather Bureau, Miami, Fla., Apr. **1959**, 10 pp.

Kasahara, Akira, "A Numerical Experiment on the Development of a Tropical Cyclone," *Journal of Meteorology*, Vol. 18, No. 3, June **1961**, pp. 259–282.

Kuo, H. L., "On Formation and Intensification of Tropical Cyclones Through Latent Heat Release by Cumulus Convection," *Journal of the Atmospheric Sciences*, Vol. 22, No. 1, Jan. **1965**, pp. 40–63.

Lilly, D. K., "A Proposed Staggered-Grid System for Numerical Integration of Dynamic Equations," *Monthly Weather Review*, Vol. 89, No. 3, Mar. **1961**, pp. 59–65.

Malkus, Joanne S., "Recent Developments in Studies of Penetrative Convection and an Application to Hurricane Cumulonimbus Towers," *Proceedings of the First Conference on Cumulus Convection, Portsmouth, N.H., May 19–22, 1959, Cumulus Dynamics*, Pergamon Press, New York, **1960**, pp. 65–84.

Miller, Banner I., "On the Momentum and Energy Balance of Hurricane Helene (1958)," *National Hurricane Research Project Report* No. 53, U.S. Weather Bureau, Miami, Fla., Apr. **1962**, 19 pp.

Molenkamp, Charles R., "Accuracy of Finite-Difference Methods Applied to the Advection Equation," *Journal of Applied Meteorology*, Vol. 7, No. 2, Apr. **1968a**, pp. 160–167.

Molenkamp, Charles R., "Reply to Comments on 'Accuracy of Finite-Difference Methods Applied to the Advection Equation,'" *Journal of Applied Meteorology*, Vol. 7, No. 5, Oct. **1968b**, pp. 938–939.

Ogura, Yoshimitsu, "The Evolution of a Moist Convective Element in a Shallow, Conditionally Unstable Atmosphere: A Numerical Calculation," *Journal of the Atmospheric Sciences*, Vol. 20, No. 5, Sept. **1963**, pp. 407–424.

Ogura, Yoshimitsu, "Frictionally Controlled, Thermally Driven Circulations in a Circular Vortex With Application to Tropical Cyclones," *Journal of the Atmospheric Sciences*, Vol. 21, No. 6, Nov. **1964**, pp. 610–621.

Ooyama, Katsuyuki, "Numerical Simulation of the Life-Cycle of Tropical Cyclones," *Contribution* No. 67, Geophysical Sciences Laboratory, Department of Meteorology and Oceanography, New York University, Dec. **1967**, 133 pp.

Ooyama, Katsuyuki, "Numerical Simulation of Tropical Cyclones With an Axi-Symmetric Model," paper presnted at the WMO/IUGG Symposium on Numerical Weather Prediction, Tokyo, Nov. 26–Dec. 4, **1968**.

Orville, Harold D., "On Mountain Upslope Winds," *Journal of the Atmospheric Sciences*, Vol. 21, No. 6, Nov. **1964**, pp. 622–633.

Palmén, E., and Riehl, Herbert, "Budget of Angular Momentum and Energy in Tropical Cyclones," *Journal of Meteorology*, Vol. 14, No. 2, Apr. **1957**, pp. 150–159.

Phillips, N. A., "A Coordinate System Having Some Special Advantages for Numerical Forecasting," *Journal of Meteorology*, Vol. 14, No. 2, Apr. **1957**, pp. 184–185.

Riehl, Herbert, and Malkus, Joanne S., "Some Aspects of Hurricane Daisy, 1958," *Tellus*, Vol. 13, No. 2, May **1961**, pp. 181–213.

Rosenthal, Stanley L., "Some Attempts to Simulate the Development of Tropical Cyclones by Numerical Methods," *Monthly Weather Review*, Vol. 92, No. 1, Jan. **1964**, pp. 1–21.

Rosenthal, Stanley L., "Numerical Experiments With a Multilevel Primitive Equation Model Designed to Simulate the Development of Tropical Cyclones: Epxeriment I," *ESSA Technical Memorandum* ERLTM-NHRL 82, U.S. Department of Commerce, National Hurricane Research Laboratory, Miami, Fla., Jan. **1969**, 36 pp.

Smagorinsky, J., "General Circulation Experiments With the Primitive Equations: I. The Basic Experiment," *Monthly Weather Review*, Vol. 91, No. 3, Mar. **1963**, pp. 99–164.

Syoño, Sigekata, "On the Vortical Rain," *Geophysical Notes*, Vol. 3, No. 25, Tokyo University, **1950**, 3 pp.

Syoño, Sigekata, "On the Structure of Atmospheric Vortices," *Journal of Meteorology*, Vol. 8, No. 2, Apr. **1951**, pp. 103–110.

Syoño, Sigekata, Ogura, Yoshimitsu, Gambo, K., and Kasahara, Akira, "On the Negative Vorticity in a Typhoon," *Journal of the Meteorological Society of Japan*, Ser. 2, Vol. 29, No. 12, Dec. **1951**, pp. 397–415.

Syoño, Sigekata, and Yamasaki, M., "Stability of Symmetrical Motions Driven by Latent Heat Release by Cumulus Convection Under the Existance of Surface Friction," *Journal of the Meteorological Society of Japan*, Ser, 2, Vol. 44, No. 6, Dec. **1966**, pp. 353–375.

Yamasaki, M., "A Tropical Cyclone Model With Parameterized Vertical Partition of Released Latent Heat," *Journal of the Meteorological Society of Japan*, Vol. 46, No. 3, June **1968**, pp. 202–214.

[*Received August 13, 1969; revised October 6, 1969*]